Unprecedented strength of Hadley circulation in 2015-2016 impacts on CO_2 interhemispheric difference

Jorgen S. Frederiksen and Roger J. Francey

CSIRO Oceans and Atmosphere, Aspendale, Victoria, AUSTRALIA

Correspondence to: Jorgen S. Frederiksen (jorgen.frederiksen@csiro.au)

Abstract. The extreme El Niño of 2015 and 2016 coincided with record global warming and unprecedented strength of the Hadley circulation with significant impact on mean interhemispheric (IH) transport of CO_2. The relative roles of eddy transport and mean advective transport on interannual differences in CO_2 concentration between Mauna Loa and Cape Grim ($C_{mlo\text{-}cgo}$), from 1992 through to 2016, are explored. Eddy transport processes occur mainly in boreal winter-spring when $C_{mlo\text{-}cgo}$ is large; an important component is due to Rossby wave generation by the Himalayas and propagation through the equatorial Pacific westerly duct generating and transmitting turbulent kinetic energy. Mean transport occurs mainly in boreal summer-autumn and varies with the strength of the Hadley circulation. The timing of annual changes in $C_{mlo\text{-}cgo}$ is found to coincide well with dynamical indices that we introduce to characterize the transports. During the unrivalled 2009-2010 step in $C_{mlo\text{-}cgo}$ the effects of the eddy and mean transport reinforce. In contrast for the 2015 to 2016 change in $C_{mlo\text{-}cgo}$ the mean transport counteracts the eddy transport and the record strength of the Hadley circulation determines the annual IH CO_2 difference. The interaction of increasing global warming and extreme El Niños may have important implications for altering the balance between eddy and mean IH CO_2 transfer. The effects of interannual changes in mean and eddy transport on interhemispheric gradients in other trace gases are also examined.

1 Introduction

Interhemispheric (IH) exchange of CO_2 occurs mainly by eddy transport in the boreal winter-spring and by mean convective and advective exchange in the boreal summer-autumn (Bowman and Cohen, 1997; Lintner et al., 2004; Miyazaki et al. 2008; and references therein).

On the basis of long-term (1949-2011) correlations of the upper-tropospheric zonal wind with the Southern Oscillation Index (SOI), Francey & Frederiksen (2016; hereafter FF16) defined an index for the Pacific westerly duct, u_{duct}, as a measure of IH eddy transport of CO_2. This index is the average zonal wind in the region 5°N to 5°S, 140°W to 170°W at 300hPa, as summarized in Table 1. In this article the period of interest is 1992 to 2016 and the corresponding correlation is shown in Figure 1S of the Supplement. There the role of the changing Walker circulation with the cycle of the El Niño-Southern

Oscillation (ENSO) in determining the properties of the Pacific and Atlantic westerly ducts is also documented. The u_{duct} index is an indicator of cross equatorial Rossby wave dispersion and associated increases in near equatorial upper tropospheric transient kinetic energy (Frederiksen and Webster, 1988), particularly between 300 and 100hPa (~9 km to ~16 km above sea level). The process normally occurs over the eastern Pacific Ocean during the boreal winter-spring and the Rossby waves (Webster and Holton, 1982; Stan et al., 2017), generated downwind of thermal anomalies and continental influences, in particular the massive Himalayan orography, propagate in a south-east direction through the Pacific westerly duct generating and transporting turbulent kinetic energy. The generation of turbulent kinetic energy occurs through Rossby wave breaking in the Pacific and Atlantic ducts and enhances turbulent mixing (Ortega et al. 2018 and references therein). FF16 also considered the relationship of u_{duct} and other trace gases including CH_4. Indeed, recently Pandey et al. (2017) and Knol et al. (2017) also considered the implications of faster IH transfer of CH_4 during the La Niña of 2011 when the Pacific westerly wind duct is open and u_{duct} is large.

FF16 explained the exceptional step in CO_2 IH difference between 2009 and 2010 as due to a contribution from the large anomaly in u_{duct} observed at the time. Recently results from the National Aeronautics and Space Administration (NASA) Orbiting Carbon Observatory-2 (OCO-2) during the 2015-2016 El Niño have been published (Chatterjee et al., 2017; and references therein) In particular release by NASA (2016) of data in a movie 'Following Carbon Dioxide through the Atmosphere' provides further direct evidence of the Pacific duct hypothesis. The NASA OCO-2 CO_2 concentration in Figure 1(a) is for 17 Feb 2015 and shows Rossby wave trains over the eastern Pacific and across South America associated with IH exchange as a typical example of OCO-2 images that coincide with the shaded 2015 period in Figure 1(b). The dynamical properties of these Rossby waves are further explored in the Supplement including Figures 3S and 4S. Figure 1(b) uses the covariance between CO_2 and u_{duct} in early 2015, indicated by shading, to predict IH CO_2 exchange through the Pacific duct. The atmospheric circulation data and indices used throughout this article are obtained from the National Centers for Environmental Prediction (NCEP) and National Center for Atmospheric Research (NCAR) reanalysis (NNR) data (Kalnay et al., 1996); in Section 6 we briefly consider the robustness of our results using another reanalysis data set. The results in Figures 1(a) and (b) are also consistent with upper-tropospheric (u, v) wind vectors. Between 5 and 23 February 2015 NNR wind vectors show that a strong Pacific North American height anomaly caused a split in the Pacific upper tropospheric winds, the Pacific westerly duct was open, and there were south-east cross equatorial winds from the Northern to Southern Hemispheres. This is illustrated in Figure 1(c) for 300 hPa wind vectors on 17 Feb 2015.

The focus here is on IH CO_2 difference, anomalies in the mean convective and advective mode of IH CO_2 exchange and changes in the relative importance of the mean and eddy transport modes.

2 Changes in CO_2 interhemispheric difference

To represent CO_2 interhemispheric difference we define $C_{mlo\text{-}cgo}$ as the difference in Commonwealth Scientific and Industrial Research Organisation (CSIRO) analysed CO_2 concentrations in baseline air sampled from Mauna Loa (mlo, 20°N, 156°W)

and Cape Grim (cgo, 41°S, 145°E). FF16 discussed the measurement and sampling strategy, consistently applied over 25 years, which has been used to establish the data set with minimum uncertainty. They also examined CO_2 interhemispheric difference using NOAA data (Dlugokencky et al. 2014) and with the Scripps Institution of Oceanography (SIO) Mauna Loa and South Pole data (Keeling et al., 2009) and found broad agreement in the two data sets, in the period of overlap since the 1990s, in terms of CO_2 changes and the relationships to the opening and closing of the Pacific westerly duct.

Figure 2 summarises annual covariations that motivated this study. In Figure 2(a) the overall trend in the $C_{mlo-cgo}$ reflects the increasing emissions, mainly in the Northern Hemisphere, of carbon from combustion of fossil fuels coupled with relatively slow transport into the Southern Hemisphere. The smooth dashed curve shows global annual anthropogenic emissions (Le Quere et al., 2017) scaled by the coefficients of linear regression between $C_{mlo-cgo}$ and emissions from 1992-2015 (0.36 ppm/PgC.yr^{-1}, n=24, r^2=0.83). The year-to-year variations in $C_{mlo-cgo}$ are more pronounced than the variations in emissions (for example only 2009, corresponding to the Global Financial Crisis, clearly interrupts the smooth emissions increase).

2.1 The influences of terrestrial fluxes and transport on interhemispheric CO_2 differences

The growth rate and concentration of atmospheric CO_2 depend on many mechanisms including fossil fuel emissions, surface fluxes, such as associated with the growth and decay of vegetation, and atmospheric mean and eddy transport. The CO_2 growth rate and IH gradients in CO_2 vary on daily, monthly, yearly and multi-year time scales where there is a quasi-periodic variability associated with the influence of ENSO (e.g. Thoning et al. 1989). This reflects the response of tropical vegetation to rainfall variations and both hemispheres are also affected through dynamical coupling.

A number of recent inversion studies have largely attributed growth anomalies in atmospheric CO_2 concentrations to anomalous responses of the terrestrial biosphere. However, the variability in the responses within Dynamic Global Vegetation Models (DGVMs) is significant. Le Quéré et al. (2017) for example note that the "standard deviation of the annual CO_2 sink across the DGVMs averages to ± 0.8 GtC yr^{-1} for the period 1959 to 2016". This is significantly larger than the reported extratropical sink anomalies during for example the major 2009-2010 step in CO_2 concentrations (Poulter et al., 2014; Trudinger et al., 2016). Francey and Frederiksen (2015) presented reasons supporting a dynamical contribution to the cause of the 2009-2010 $C_{mlo-cgo}$ step.

For the 2015-2016 period of particular relevance here there are two studies that stand out. Keenan et al. (2016) interpret slowing CO_2 growth in 2016 as strong uptake by Northern Hemisphere terrestrial forests. Yue et al. (2018) examine the reasons for the strong positive anomalies in atmospheric CO_2 growth rates during 2015. They present evidence of the Northern Hemisphere terrestrial response to El Niño events by way of satellite observations of vegetation greenness. To reconcile increased greenness with increased CO_2 growth their inversion modelling requires the "largest ever observed" transition from sink to source in the tropical biosphere at the peak of the El Niño, "but the detailed mechanisms underlying such an extreme transition remain to be elucidated".

In this study, we find that the 2015-2016 El Niño also corresponds to unprecedented anomalies in both mean and eddy IH CO_2 transport characterized by indices of these transfers that we introduce, affecting Northern Hemisphere CO_2 growth. As

for the anomalies in CO_2 IH gradient during the 2009-2010 El Niño, studied in FF16, this again suggests a contributing role for anomalous IH transport during the 2015-2016 event. We examine this possibility in detail and study the relationships between the extremes in IH CO_2 differences and transport anomalies for 1992 to 2016 and associated correlations between $C_{mlo\text{-}cgo}$ (and other trace gases) and dynamical indices of transport.

2.2 Dynamical influences on IH exchange

Figure 2(b) confirms that much of the year-to-year variability in $C_{mlo\text{-}cgo}$, particularly preceding 2010, occurs in the boreal winter-spring (Dec-May) when eddy transport is expected to be the more active contribution to IH exchange (FF16). The step jump in annual values between 2009 and 2010 that was the focus of FF16, is the most prominent feature. A similar relationship with u_{duct} is supported prior to 2010 as indicated here by vertical dashed gridlines aligned with the beginning of the calendar years when u_{duct} is unusually low ($u_{duct} \leq 3ms^{-1}$). At these times u_{duct} generally corresponds to above-average $C_{mlo\text{-}cgo}$, consistent with an accumulation of CO_2 in the Northern Hemisphere at a time when the Pacific duct transfer is small.

A notable exception occurs in 2015-2016 and this is a particular focus of this study that we address in the context of the unusual $C_{mlo\text{-}cgo}$ behaviour since 2010. For example, since 2010 the annual average $C_{mlo\text{-}cgo}$ in Figure 2(a) shows reduced scatter and a slight decrease at a time when fossil fuel emissions continue to grow. As shown in Figure 2(b), this $C_{mlo\text{-}cgo}$ decrease is more marked in the boreal summer-autumn (Jun-Nov) than in boreal winter-spring (Dec-May) when it is relatively stable (and even recovers in the last 3 years).

The steadily decreasing u_{duct} since 2012 occurs all year round in Figure 2(c). Similar but more marked decreases occur in indices ω_H and v_H in Figure 2(d), which measure the strength and location of the Hadley circulation. Here, ω_H is the 300 hPa vertical velocity in pressure coordinates ($\omega = dp/dt$ where p is pressure) averaged zonally (0-360°) and between 10°N and 15°N (Table 1). Also, v_H is the 200 hPa south-to-north meridional wind averaged zonally and between 5°N and 10°N (Table 1). Both ω_H and v_H become more negative and the mean transport from the Northern to Southern Hemispheres increases with a strengthening of the Hadley circulation. As noted by Freitas et al. (2017; and references therein) the Hadley circulation strengthens during El Niños, and particularly for strong events such as during 2015-2016 (L'Heureux et al., 2017). There are subtle relationships between the latitudinal width of the equatorial heating during El Niño and global warming (Freitas et al., 2017) and the Hadley circulation. However, it is expected that there will be an increasing frequency of extreme El Niño events with increasing global warming (Cai et al., 2014; Yeh et al., 2018).

Before examining the Hadley component further, we clarify factors associated with the eddy transfer through the Pacific duct.

3 The role of the Pacific westerly duct in IH CO_2 eddy transport

We examine here the concept of relatively rapid interhemispheric CO_2 exchange through a spatially restricted Pacific duct and discuss issues of the uniqueness of the duct and the transport of both turbulent kinetic energy and CO_2 to and through the Pacific duct region.

3.1 Eddy generation in the equatorial zone

The u_{duct} zonal wind based on the peak climatological correlation with SOI (140°W -170°W) is also largely representative of near equatorial (5°N to 5°S) zonal winds and their variability in the larger region between 90°W and 180°. Pattern correlations between the two vary from $r \sim 0.9$ for November to April to $r \sim 0.7$ for May to October.

In Figure 3, Hovmoller diagrams for the Western Hemisphere (180° to 0°W) between 2008 and 2016 show the time-longitude of daily 300hPa zonal winds between 5°N and 5°S. The cool blue background represents easterly winds (negative u) while warm colours, green to yellow through to red, depict westerlies (positive u). Frederiksen and and Webster (1988) found that near equatorial upper tropospheric transient kinetic energy generation is approximately linearly related to zonal wind strength (their Figure 6) and is strongest for westerlies when the winds oppose the earth's rotation. The longitudinal limits of u_{duct} determined from the SOI correlation are enclosed by solid white rounded rectangles in Figure 3, while the time period (rectangle height) represents those months when $C_{mlo\text{-}cgo}$ is at a seasonal maximum and winds in the Pacific duct are normally westerly (Feb-Apr).

In most years, u_{duct} is positive in boreal winter-spring and Rossby waves generated by, for example, the Himalayas (height of 8.8 km) can propagate through the downstream Pacific duct region (140°W -170°W, 5°N-5°S) producing and transporting turbulent kinetic energy southwards. In some years, such as the boreal winter-spring of 2009-2010 and 2015-2016, u_{duct} is anomalously weak and the peak equatorial 300 hPa zonal winds are over the Atlantic ocean, particularly in the Atlantic duct region defined as 10°W-40°W, 5°N-5°S. The Atlantic duct region, most conspicuously, is downstream of the Rockies (height of 4.4 km). Figure 1S of our Supplement and Figure 4(a) of FF16 show that the SOI and Atlantic duct zonal winds are strongly *anti-correlated* in contrast to the strong correlation with u_{duct}; as well, in the Eastern Hemisphere the correlation between the SOI and equatorial zonal winds is quite weak. We note that u_{duct} and the Atlantic duct winds are anti-correlated with $r = -0.66$. Further while u_{duct} is anti-correlated with $C_{mlo\text{-}cgo}$ the Atlantic duct winds are correlated with a similar magnitude. This indicates that changes in u_{duct} are the primary determinant of interhemispheric CO_2 duct transfer via eddy processes and $C_{mlo\text{-}cgo}$ and the opening of the Atlantic duct is mainly important through the associated closing of the Pacific duct. This is consistent with the idea that Rossby wave dispersion from the smaller topographic features of the Rockies is less important than from the more massive Himalayas, as further discussed in the Supplement.

3.2 Transport of surface CO_2 emissions to the upper troposphere

Transport of CO_2 emissions from the surface to the upper troposphere is explored next. We find that when the Pacific duct is open there is also large scale uplift slightly downstream of Asia so that in a given winter-spring season the substantial regional emissions are effectively transported directly through the duct via Rossby wave dispersion, including by the Himalayan wave train. Figure 4 shows the Feb-Apr correlation between the 500hPa ω (the vertical wind in pressure coordinates with negative values corresponding to uplift in height coordinates) and the SOI from 1948 to 2016. The most prominent correlations occur within ±30°of the equator at longitudes 120°E to 170°W, upstream and at the longitudes of the Pacific duct and this is in fact the case at all levels between the surface and 100 hPa (not shown). Broadly similar correlations are obtained between the 500 hPa ω and u_{duct} for Feb-Apr (and for 500 hPa ω and SOI for Jan-Dec). At other times, for example in 2010 and 2015-2016, when there have been persisting easterlies in the Pacific duct region there has been descent slightly downstream of the Asian region. Thus the recent record Asian emissions may play a significant role in direct episodic IH CO_2 transfer through the Pacific duct. To the extent that Asian emissions might be preferentially represented in direct IH CO_2 transfer, it is relevant that uncertainty and possibly variability in Asian emissions are greater than the reported uncertainty and variability in the global totals (Andres et al., 2014).

4 The role of the Hadley circulation in mean IH CO_2 transport

As noted in Section 2, the years 2010 and 2016 exhibit a similar anomalous eddy transport index, u_{duct}, but have different $C_{mlo\text{-}cgo}$ responses relative to previous years (Figure 2(a)). Since the CO_2 emitted in the Northern Hemisphere and tropics is also transported into the Southern Hemisphere by the mean divergent flow associated with the Hadley circulation, particularly during boreal summer (Miyazaki et al., 2008)**,** this is now explored in more detail. The Pacific duct transfer in boreal winter-spring, with peaks in Feb-Apr, occurs when the CO_2 IH partial pressure difference is near maximum due to forest respiration. Likewise the mean IH transport related to the Hadley circulation occurs in boreal summer-autumn, with peaks in Jun-Aug, when the CO_2 IH partial pressure difference has a proportionally larger contribution due to the accumulated fossil fuel CO_2 from NH industrial emissions.

Figure 5 shows latitude-height cross sections, over the Pacific, averaged between 120°E-240°E, of June to August vertical wind in pressure coordinates, ω, while Figure 6 shows the corresponding results for the meridional wind, v. Recall that negative ω corresponds to positive vertical velocity in height coordinates and negative v is north-to-south meridional wind. In the boreal summer-spring average values for 1979 to 2016 show the uplift (negative ω) at low northern latitudes (Figure 5(a)) while the advective Hadley Cell meridional transfer (negative v) to the Southern Hemisphere at high altitude can be seen in Figure 6(a).

By subtracting the 1979-2016 average from the 2016 ω values and v values, the nature of the extreme 2016 anomaly becomes visible, with strong uplift including between 10°N and 15°N shown in Figures 5(b) and extensive meridional wind penetration into the Southern Hemisphere, particularly between 500hPa and 300hPa, shown in Figure 6(b).

Figures 5(c) and 6(c) depict the difference between the anomaly years 2016 and 2010. Both the uplift between 10°N and 15°N and penetration of the meridional wind into the Southern Hemisphere is stronger in the upper troposphere and mean transport through convection and advection into the Southern Hemisphere more extensive in 2016.

On the basis of these figures, and similar figures for the corresponding zonally averaged quantities, we have chosen four indices to characterize the mean circulation by the Hadley Cell (Table 1). These are ω_P the vertical velocity in pressure coordinates over the Pacific ocean at 300 hPa averaged between 120°E-240°E and 10°N-15°N, v_P the meridional wind at 200hPa averaged between 120°E-240°E and 5°N-10°N as well as the corresponding zonally averaged indices ω_H and v_H introduced in Section 2.

5 Quantifying the $C_{mlo\text{-}gco}$ relationships with eddy and mean transport indices

The timing of a majority of short term variations in the 25-year baseline $C_{mlo\text{-}cgo}$ corresponds to atmospheric transport changes that influence the interhemispheric exchange. To quantify relationships between $C_{mlo\text{-}cgo}$ and the eddy and mean transport indices involved we first suppress the $C_{mlo\text{-}cgo}$ changes expected from reported anthropogenic emissions. The global annual average anthropogenic emissions (Le Quere et al., 2017) are converted to ppm using the coefficient 0.36 ppm/PgCyr^{-1} derived in Section 2 from Figure 2 and subtracted from the observed $C_{mlo\text{-}cgo}$. In Figure 6 we compare the FF-adjusted $C_{mlo\text{-}cgo}$, which we denote $C^*_{mlo\text{-}cgo}$, for two periods when $C_{mlo\text{-}cgo}$ is positive; the first is Feb-Apr that best captures the eddy IH exchange, and the second is Jun-Aug when mean transfer related to the Hadley circulation is captured.

We focus first on the FF-adjusted $C^*_{mlo\text{-}cgo}$ plots in Figures 7(a) and (b). The mean and year-to-year variation is very much larger in (a) compared to (b) and is also larger in (a) compared to the annual averaged values in Figure 2(a). The contrasting behaviour between the two periods after 2012 is also more marked.

To emphasize the similarities between $C^*_{mlo\text{-}cgo}$ and Pacific duct winds we plot $-u_{duct}$ in Figure 7(a), so that easterlies are shown as positive and the more frequent westerlies as negative; the timings of peaks in both panels then correspond. When winds in the Pacific duct are easterly or near zero, FF-adjusted $C^*_{mlo\text{-}cgo}$ peak or are above average; this is now more obvious in 2016 compared with the corresponding results for $C_{mlo\text{-}cgo}$ in Dec-May shown in Figure 2(b) and 2(c). In fact the FF-adjusted $C^*_{mlo\text{-}cgo}$ has very similar behaviour to the detrended $C_{mlo\text{-}cgo}$, with pattern correlations of anomalies of $r = 0.931$, $r = 0.954$ and $r = 0.981$ for Jan-Dec, Jun-Aug and Feb-Apr respectively. The similarity can also be seen by comparing the top panel of Figure 7(b) with that of Figure 8. Despite persistent agreement in timing, the magnitude of the $C_{mlo\text{-}cgo}$ response to the u_{duct} anomaly is more variable. This is reflected in the correlation between the detrended $C_{mlo\text{-}cgo}$ anomalies and the detrended u_{duct} anomalies which is $r = -0.500$ for Feb-Apr and $r = -0.228$ for Dec-May. These results confirm the preferential Pacific duct transfer in late boreal winter and early spring (Feb-Apr). They also indicate that although there is

an important relationship between $C_{mlo-cgo}$ and the zonal wind in the Pacific duct, other processes detailed in Section 2, such as changes in direct advective transport by the mean winds and emissions, also play roles in year-to-year IH variations. This is also confirmed by a regression analysis of $C_{mlo-cgo}$ anomalies onto u_{duct} anomalies (not shown) where there is significant scatter about the regression line.

In particular, during 2009-2010 there were a number of complicating factors that most likely contributed. The unusually low $C_{mlo-cgo}$ in 2008, 2009 coincide with the Global Financial Crisis when global emissions dipped (and recent British Petroleum, 2018, estimates of emissions suggest an even larger 2008-2009 anomaly than in data used here). Terrestrial Net Biosphere Production south of 30°S was also anomalously low in 2009 and anomalously high in 2010 (FF16; Trudinger et al. 2016; though by amounts not sufficient to impact on the Cape Grim baseline CO_2 records). The low $C_{mlo-cgo}$ also align with near-record strong westerlies in the Pacific duct, and associated larger eddy transport, in 2008; both potentially contribute to increasing the magnitude of the subsequent CO_2 step.

In Figure 7(b) the post-2010 decrease in Jun-Aug FF-adjusted $C^{*}_{mlo-cgo}$ is clearly mirrored in the decreasing ω and v indices (indicating strengthened Hadley circulation) , particularly in the 120°E-240°E Pacific sector (ω_P and v_P) compared to the zonal average (ω_H and v_H). The considerably weaker strength of the Hadley circulation in 2010 compared with 2016 is shown quite distinctly. The correlations between the detrended $C_{mlo-cgo}$ anomalies and indices of mean transport are shown in Table 2.

Generally Jun-Aug correlations are stronger than the Jun-Nov correlations and correlations over the Pacific sector 120°E-240°E are generally larger than for the zonally averaged quantities. This is clearly the case for ω while v_H is an exception being larger for the longer time period. The $C_{mlo-cgo}$ correlations for Jun-Aug involving ω_P and v_P have roughly similar magnitudes to those for Feb-Apr involving u_{duct} and ω_P and v_P provide similar predictability of the role of the Hadley circulation in mean IH CO_2 transport as u_{duct} does for eddy transport. Interestingly, during 2009-2010 the effects of u_{duct} and ω_P and v_P reinforce to make the step in $C_{mlo-cgo}$ large, while for 2015-2016 ω_P and v_P counteract u_{duct} and the exceptionally strong Hadley circulation becomes the dominant feature in determining the annual $C_{mlo-cgo}$ (Figure 1a). These results show that there is an important connection between the $C_{mlo-cgo}$ and the indices that characterize the strength of the Hadley circulation and mean transport. Again, as also suggested by regression analysis (not shown), other processes, detailed in Section 2 and above, also play important roles.

The somewhat different behaviours of $C_{mlo-cgo}$ and the dynamical indices, particularly during the El Niños of 2009-2010 and 2015-2016 and of 1997-1998, may partly reflect the diversity of El Niños and whether the heating is focussed in the Eastern Pacific or in the Central Pacific (Capotondi et al. 2015; L'Heureux et al. 2017 and references therein). The strong 1997-1998 event like, the 1982-1983 event, was a classic Eastern Pacific El Niño with maximum temperature anomalies there of nearly $+4^{o}$ C (L'Heureux et al. 2017). The 2009-2010 event in contrast was a Central Pacific El Niño with record-breaking warming in the central Pacific (Kim et al. 2011). The 2015-2016 El Niño fell between these two canonical cases with less warming in the eastern Pacific Ocean than the 1997-1998 event but similar warming to the 2009-2010 event in the central Pacific (L'Heureux et al. 2017).

The broadly increasing magnitude of the negative ω and v indices since 2012 is associated with both increasing global temperatures, breaking the record in 2016, and the large El Niño of 2015 and 2016. This has resulted in the increasing importance of the mean convective and advective CO_2 transport by the Hadley circulation relative to the eddy transport including through the Pacific duct. It will be interesting to see whether this favouring of the mean over the eddy IH CO_2 transport will become increasingly important with further global warming and the extent to which it depends on extreme El Niños (Cai et al., 2014; Freitas et al., 2017; Yeh et al., 2018)**.**

The dynamical indices that we have used for this study are based on the NCEP-NCAR reanalysis (NNR) data (Kalnay et al. 1996). There is generally close correspondence between the major global atmospheric circulation data sets that, like the NNR data, use full data assimilation throughout the atmosphere (Frederiksen & Frederiksen 2007; Frederiksen et al. 2017; Rikus 2018). We have confirmed this by recalculating our dynamical indices and main correlations with $C_{mlo\text{-}cgo}$ based on the NASA Modern Era Retrospective-analysis for Research and Applications (MERRA) data (Rienecker et al. 2011). For example, the 1992 to 2016 correlation between MERRA and NNR data for u_{duct} in Feb-Apr is $r = 0.974$, for ω_P in Jun-Aug is $r = 0.899$ and for v_P in Jun-Aug is $r = 0.931$. The corresponding correlations between detrended anomalies of $C_{mlo\text{-}cgo}$ and the MERRA based dynamical indices are also very similar. The correlations are $r = -0.512$ with u_{duct} for Feb-Apr (compared with $r = -0.500$ for the NNR index), $r = 0.504$ with ω_P for Jun-Aug (compared with $r = 0.522$ based on NNR) and $r = 0.538$ with v_P for Jun-Aug (compared with $r = 0.539$ based on NNR).

6 Interhemispheric exchange of other trace gases

Next, we consider the eddy and mean IH exchange of other trace gas species and their correlations with CO_2 and dynamical indices of transport. We focus on Feb-Apr for eddy transport and Jun-Aug for mean transport since these periods were the peaks for correlations of CO_2 IH difference with eddy and mean transport indices respectively. However, there are differences in the seasonal variability of interhemispheric gradient in the different trace gas species that are reflected in their transport and for that reason we also briefly mention the results for other time periods. We begin by further examining Mauna Loa minus Cape Grim (mlo–cgo) differences, between 1992-2016, in the routinely monitored CSIRO species CH_4, CO and H_2 in addition to CO_2 that were briefly considered in Frederiksen and Francey (FF16), as well as N_2O (for 1993-2016). Thereafter we discuss mlo–cgo differences in SF_6 data sourced from the NOAA Halocarbons and other Atmospheric Trace Species Group (HATS) program from 1998 (NOAA, 2018).

6.1 Pacific westerly duct and eddy IH transport of CSIRO monitored trace gases

The IH exchange of the trace gas species, CH_4, CO and H_2, in addition to CO_2, and the role of the Pacific westerly wind duct were also considered in FF16. In particular, the covariance, of the mlo–cgo difference in these routinely monitored CSIRO species with u_{duct}, is shown in Figure 5 of FF16. We recall that the u_{duct} index is the average zonal wind in the region 5°N to 5°S, 140°W to 170°W at 300hPa. As noted in FF16, the extreme cases of Pacific westerly duct closure in 1997–98 and

2009–10 show up in the reduction of seasonal IH exchange for CH_4 and CO as well as CO_2. The similar behaviour of detrended anomalies of mlo–cgo difference in CH_4, CO and CO_2 and their correlations with u_{duct} is shown in Table 3 for Feb–Apr. We note the quite high correlations of CH_4 and CO with CO_2 ($r = 0.697$ and $r = 0.645$ respectively) and the significant anti–correlations of all these three species with u_{duct} ($r = -0.448$, $r = -0.605$ and $r = -0.500$ respectively). In fact, for Mar-May the correlation between CH_4 and CO_2 is even larger at $r = 0.728$ (and with u_{duct} it is $r = -0.474$) while between CO and CO_2 it is $r = 0.611$ (and with u_{duct} it is $r = -0.507$). These results are of course consistent with Figure 5 of FF16 and are further evidence of similarities of IH transient eddy transport of these three gases. Table 3 also shows that the Feb-Apr correlation of H_2 with CO_2 and anti–correlation with u_{duct} have smaller magnitudes ($r = 0.296$ and $r = -0.218$ respectively). These results for anomalies are probably related to corresponding similarities and differences in the seasonal mean values (not shown) of these gases in Feb–Apr, as discussed below.

Anomalies in mlo–cgo differences in CSIRO monitored N_2O are generally poorly correlated with those in CO_2 as shown for Feb-Apr and Jun-Aug in Tables 3 and 4 respectively (the maximum 3 month average correlation is $r = 0.274$ for Mar-May) and this is mirrored in generally poor correlation with the dynamical indices shown in Tables 3 and 4. This reflects the fact that natural exchanges with equatorial agriculture and oceans are the main sources (Ishijima et al., 2009), and the seasonal range in mlo-cgo difference is only around 0.2% of the mean N_2O level, more than 10 times less than is the case for the other species.

6.2 Hadley circulation and mean IH transport of CSIRO monitored trace gases

We examine the role of the Hadley circulation on the mean transport of trace gases focusing on the boreal summer period of Jun–Aug. Table 4 shows the correlations between the detrended anomalies of mlo–cgo difference in CH_4, CO and H_2 with CO_2 and with the dynamical indices ω_P and v_P (Table 1). We note that the largest Jun-Aug correlation is between H_2 and CO_2 ($r = 0.680$) and the correlations between CH_4 and CO with CO_2 are considerably smaller ($r = 0.246$ and $r = 0.108$ respectively) while for Apr-Jun the latter correlations are more comparable at $r = 0.583$ and $r = 0.496$ respectively. These correlations with CO_2 are also reflected in the respective correlations of the other trace gases with ω_P and v_P. We note from Table 4 that the Jun-Aug correlations of H_2 with ω_P and v_P are $r = 0.427$ and $r = 0.442$ respectively which is slightly less than the corresponding correlations between CO_2 and the dynamical indices ($r = 0.522$ and $r = 0.539$ respectively) but considerably larger than for CH_4 and CO. For May-Jul the correlation of H_2 with ω_P is slightly larger with $r = 0.526$.

Again, the different behaviour of the trace gas anomalies may be related to their different seasonal mean values; the seasonal mean IH difference for H_2 peaks in boreal summer while for CH_4 and CO it is relatively low with a minimum in August. The distribution and variability of surface exchange is different for each of the trace gases and there is potential for this to interact with the restricted extent and seasonal meandering of the regions of uplift to influence IH exchange of a species. For example, 70% of the global total CH_4 emissions are from mainly equatorial biogenic sources that include wetlands, rice

agriculture, livestock, landfills, forests, oceans and termites (Denman et al., 2007) and CO emissions contain a significant contribution from CH_4 oxidation and from tropical biomass burning.

A more detailed examination of the inter–annual variation of the mlo–cgo difference in H_2 during boreal summer is presented in Figure 8. It shows the detrended H_2 data in comparison with the corresponding CO_2 data and with the ω_P and v_P indices. First we note that the detrended CO_2 data in the top panel has very similar inter–annual variation to the FF–adjusted $C^*_{mlo\text{-}cgo}$ in Figure 7(b). We also see that the qualitative behaviour of H_2 mirrors many aspects of CO_2, as expected from the correlations in Table 4. In particular, the increase in the IH difference of H_2 in 2010 is even more pronounced than for CO_2. For CO_2 and for H_2 there is a steady reduction in the IH difference from around 2013 leading to a local minimum in 2016. In both of these respects these gases broadly follow the changes in the Hadley circulation including the strengthening during 2015–2016. Vertical lines in Figure 8 indicate other times between 1992 and 2016 when transitions occur in both these trace gases and in the Hadley circulation characterized by ω_P and v_P.

Surface exchanges of H_2 have similarities to those of CO_2 in that they occur mostly at mid–northern latitudes and are mainly due to emissions from fossil fuel combustion. However H_2 also has mid–northern latitude photochemical sources peaking in August (Price et al., 2007). These boreal summer sources are almost offset by a combined soil and hydroxyl sink, but the overall interhemispheric partial pressure difference is boosted by a significant reduction in the Southern Hemisphere photochemical source at that time. For both species, the most northern excursions of the inter–tropical convergence zone that occurs at Pacific latitudes encounter increasing concentrations of both gases.

As noted above, anomalies in mlo–cgo differences in N_2O are poorly correlated with those in CO_2 and in dynamical indices (Tables 3 and 4). Indeed the 3 month average anti-correlation with u_{duct} that has the largest magnitude is $r = -0.133$ for Mar-May and the largest correlations with ω_P is $r = 0.359$ for Apr-Jun and with v_P is $r = 0.350$ for May-Jul.

6.3 Interhemispheric exchange of SF_6

In the case of SF6 we have analysed the mlo–cgo difference in available NOAA HATS data from 1998 to 2012 when cgo HATS measurements ceased. Correlations (Tables 3 and 4) of detrended anomalies in IH differences in SF_6 with those in CO_2 are as follows: the Feb–Apr correlation is $r = 0.619$, the Mar-May correlation is $r = 0.722$, the Apr-Jun correlation is $r = 0.595$, the May–Jul correlation is $r = 0.303$ and the Jun–Aug correlation is $r = 0.223$. The corresponding correlations with dynamical indices are as follows: for Feb–Apr the correlation with u_{duct} is $r = -0.617$, the May–Jul correlations with ω_P is $r = 0.465$, the Jun–Aug correlation with ω_P is $r = 0.433$, the May–Jul correlation with v_P is $r = 0.517$ and the Jun–Aug correlation with v_P is $r = 0.385$. We note that SF_6 has an anti-correlation with u_{duct} for Feb-Apr that has larger magnitude than for CO_2 and even CO. Thus, there is again a significant influence of the Pacific westerly duct, in late boreal winter and spring, and of the Hadley circulation, in boreal summer and late spring, as measured by these indices, on the mlo–cgo differences of SF_6; these SF_6 differences exhibit a similar step change in 2009-2010 as shown for CO_2 in Figures 2 and 7.

7 Conclusions

The major El Niño of 2015 and 2016 coincided with record global warming, with 2016 having the highest global average surface temperatures and 2015 the third highest (2017 had the second highest). The strength of the Hadley circulation also increased to unprecedented levels during 2015-2016 and had a major impact on the mean interhemispheric (IH) transport of CO_2 and on the difference in CO_2 concentration between Mauna Loa and Cape Grim ($C_{mlo\text{-}cgo}$). This study has focussed on the roles of IH transient eddy and mean transport of CO_2 on interannual variations in $C_{mlo\text{-}cgo}$ and has established dynamical indices that characterize the broad features of this transfer (Table 1). Interestingly, some of these indices are based on regions that lie close to or overlap the region of the Niño 3.4 SST index (5°N-5°S, 120°W-170°W) where ENSO is strongly coupled to the overlying atmosphere (L'Heureux et al., 2017).

One of these indices, u_{duct} , which is a measure of eddy IH transport of CO_2, was introduced in FF16. This index is the 300 hPa Pacific zonal wind averaged between 5°N-5°S and 140°W-170°W and is strongly correlated with the Southern Oscillation (SOI) index ($r\sim0.8$ in Figure 4(a) of FF16). A particular focus of that study was to propose an explanation for the record step in CO_2 IH difference between 2009 and 2010 and it was concluded that the closing of the Pacific duct (negative u_{duct}) during the El Niño of 2010 was a significant contributing factor. It was also noted that there were half a dozen other occasions going back to the 1960s when the closing of the Pacific duct was related to an increase in CO_2 IH difference (Keeling et al., 2009).

Here, we have extended the analysis of the relationship between u_{duct} and $C_{mlo\text{-}cgo}$ to 2016. We again find that during boreal winter-spring, and particularly during Feb-Apr when eddy transport of CO_2 from the Northern to Southern Hemispheres is most active, there is an increase in $C_{mlo\text{-}cgo}$ during the El Niño of 2015-2016. However, while the timing of the increases in these years, and for other occasions going back to 1992, agree with the closing of the Pacific duct the magnitude is more variable indicating the contribution of other processes discussed in Section 2. We have analysed the intermittent nature of the opening and closing of the Pacific westerly duct. In particular, episodes in February 2015 have been related to results from NASA (2016) data in the movie 'Following Carbon Dioxide through the Atmosphere'. The movie provides further evidence of the propagation of Rossby waves through the open Pacific westerly duct and the transfer of CO_2 into the Southern Hemisphere. We have also noted that large scale uplift slightly downstream of Asia occurs when the Pacific duct is open allowing these substantial emissions to be transported directly, via Rossby wave dispersion, through the duct.

A major focus of this article has also been the role of changes in the mean IH CO_2 transport from the Northern to Southern Hemispheres due to variability in the Hadley circulation. We have introduced indices (Table 1) that measure this transfer based on the 300 hPa ω, the vertical velocity in pressure coordinates, between 10°N and 15°N and 200 hPa v, the meridional wind between 5°N and 10°N, both zonally averaged (ω_H and v_H) and with averaging restricted to the Pacific sector 120°E-240°E (ω_P and v_P). The correlations for Jun-Aug between $C_{mlo\text{-}cgo}$ and ω_P or v_P ($r\sim0.5$) have roughly similar magnitudes to those in Feb-Apr involving u_{duct}. The indices ω_P and v_P provide similar predictability of the role of the Hadley circulation in mean IH CO_2 transport as u_{duct} does for eddy transport. We have also found that, during 2009-2010 the effects of

u_{duct} and ω_P and v_P reinforce to make the step in $C_{mlo\text{-}cgo}$ large. In contrast, for 2015-2016 ω_P and v_P counteract u_{duct} and the record Hadley circulation primarily determines the annual Mauna Loa and Cape Grim CO_2 difference. The effects of interannual changes in mean and eddy transport on IH gradients in CO_2 (and CH_4, CO, H_2, N_2O and SF_6) has been examined for the period 1992 to 2016.

The sign and strength of zonal winds in the Pacific westerly duct (u_{duct}) are related to Rossby wave dispersion and breaking and are correlated with corresponding changes in near-equatorial transient kinetic energy (Fig. 6, Frederiksen and Webster 1988) resulting in intermittent changes in the mixing of trace gases. This effect may not be adequately represented in the parameterizations (Frederiksen et al. 2016) used in atmospheric circulation and transport models. Model determinations of short term variations in the Hadley circulation exchange are also susceptible to uncertainties in representations of the equatorial convective dynamics (Lintner et al. 2004). Over at least 25 years, much of the variability in CO_2 between the two surface monitoring sites of Mauna Loa and Cape Grim can be associated with dynamical near-equatorial atmospheric indices of global significance in a changing climate. The changing nature of the seasonal and inter annual changes in CO_2 IH Pacific duct eddy and mean Hadley circulation transfer between 1992 through to 2016 provides an interesting case study and potential test of inversion models of atmospheric transport.

We plan to further explore trace gas IH transfer focussing on Southern Hemisphere CO_2 stable isotope data in a study that distinguishes between mean IH transfer and eddy transfers of both current season emissions and accumulated Northern Hemisphere fossil fuel emissions.

Data availability. Meteorological data is available from the NOAA/ESRL web site: http://www.esrl.noaa.gov/psd/ and from the NASA web site: https://giovanni.gsfc.nasa.gov/giovanni/ and trace gas data is available upon request from the corresponding author (jorgen.frederiksen@csiro.au).

Author contributions. J. S. Frederiksen provided information on atmospheric dynamics and the roles of transport mechanisms and R. J. Francey provided the trace gas information. Both contributed to the writing of the paper.

Competing interests. The authors declare that they have no conflicts of interest.

Acknowledgements. We thank Nada Derek and Stacey Osbrough for assistance with the graphics and Paul Steele has provided valuable advice on the manuscript. The sustained focus and innovation of CSIRO GASLAB personnel, and skilled trace gas sample collection by personnel at the Bureau of Meteorology Cape Grim Baseline Atmospheric Program and NOAA's Mauna Loa stations underpin the progress reported here. The dynamics contributions were prepared using data and software from the NOAA/ESRL Physical Sciences Division web site: http://www.esrl.noaa.gov/psd/ except, as stated in Section 6, where NASA MERRA data was also used from the web site: https://giovanni.gsfc.nasa.gov/giovanni/. We acknowledge NASA Goddard Flight Center and their Production Team for the movie 'Following Carbon Dioxide through

the Atmosphere' available at the web site: https://svs.gsfc.nasa.gov/12445. The trace gas data for CSIRO monitored species CO_2, CH_4, CO, H_2 and N_2O and the NOAA monitored SF_6 are available from the World Data Centre for Greenhouse Gases website: https://ds.data.jma.go.jp/gmd/wdcgg/cgi-bin/wdcgg/catalogue.cgi.

References

1. Andres, R. J., Boden, T. A., & Higdon D.: A new evaluation of the uncertainty associated with CDIAC estimates of fossil fuel carbon dioxide emission, Tellus B 66, 23616, 2014.
2. Bowman, K. P., & Cohen, P. J.: Interhemispheric exchange by seasonal modulation of the Hadley circulation, J. Atmos. Sci., 54, 2045-2059, 1997.
3. British Petroleum: CO_2 emissions, 2018. https://www.bp.com/en/global/corporate/energy-economics/statistical-review-of-world-energy/co2-emissions.html
4. Cai, W., Borlace, S., Lengaigne, M., van Rensch, P., Collins, M., Vecchi, G., Timmermann, A., Santoso, A., McPhaden, M. J., Wu, L., England, M. H., Wang, G., Guilyardi, E., & Jin, F. F. : Increasing frequency of extreme El Niño events due to greenhouse warming, Nature Climate Change, 4, 111-116, doi:10.1038/nclimate2100, 2014.
5. Capotondi, A., Wittenberg, T., Newman, M., Lorenzo, E. D., Yu, J. Y., Braconnot, P., Cole, J., Dewitte, B., Giese, B., Guilyardi, E., Jin, F. F., Karnauskas, K., Kirtman, B., Lee, T., Schneider, N., Xue, Y., & Yeh, S. W.: Understanding ENSO diversity, Bull. Amer. Meteor. Soc., 96, 921–938, doi: 10.1175/BAMS-D-13-00117.1, 2015.
6. Chatterjee, A., Gierach, M. M., Sutton, A. J., Feely, R. A., Crisp, D., Eldering, A., Gunson, M. R., O'Dell, C. W., Stephens, B. B., & Schimel, D. S.: Influence of El Niño on atmospheric CO2 over the tropical Pacific Ocean: Findings from NASA's OCO-2 mission, Science, 358, eaam5776, doi:10.1126/science.aam5776, 2017.
7. Denman, K. L., Brasseur, G., Chidthaisong, A., Ciais, P., Cox, P. M., Dickinson, R. E., Hauglustaine, D., Heinze, C., Holland, E., Jacob, D., Lohmann, U., Ramachandran, S., da Silva Dias, P. L., Wofsy, S. C., & Zhang, X.: Couplings Between Changes in the Climate System and Biogeochemistry. In: *Climate Change 2007: The Physical Science Basis. Contribution of Working Group I to the Fourth Assessment Report of the Intergovernmental Panel on Climate Change* [Solomon, S., Qin, D., Manning, M., Chen, Z., Marquis, M., Averyt, K.B., Tignor, M. & Miller, H.L. (Eds.)]. Cambridge University Press, Cambridge, United Kingdom and New York, NY, USA, 2007.
8. Dlugokencky, E. J., Lang, P.M., Masarie, K.A., Crotwell, A.M., and Crotwell, M.J.: Atmospheric Carbon Dioxide Dry Air Mole Fractions from the NOAA ESRL Carbon Cycle Cooperative Global Air Sampling Network, 1968-2013, Version: 2014-06-27, 2014. Path: ftp://aftp.cmdl.noaa.gov/data/trace_gases/co2/flask/surface/
9. Francey, R. J., & Frederiksen, J. S.: Response to Poulter (Biogeosciences Discuss., 12, C7009-C7011, 2015), Biogeosciences Discuss., 12, C7771, Supplement, 2015. http://www.biogeosciences-discuss.net/12/C7771/2015/bgd-12-C7771-2015-supplement.pdf

10. Francey, R. J., & Frederiksen, J. S.: The 2009–2010 step in atmospheric CO_2 interhemispheric difference, Biogeosciences, 13, 873- 885, doi: 10.5194/bg-13-873-2016, 2016.
11. Freitas, A. C. V., Frederiksen, J. S., O'Kane, T. J., & Ambrizzi, T.: Simulated austral winter response of the Hadley circulation and stationary Rossby wave propagation to a warming climate, Clim. Dyn., 49, 521–545, doi: 10.1007/s00382-016-3356-4, 2017.
12. Frederiksen, C. S., Frederiksen, J. S., Sisson, J. M., & Osbrough, S. L.: Trends and projections of Southern Hemisphere baroclinicity: The role of external forcing and impact on Australian rainfall, Clim. Dyn., 48, 3261–3282, doi: 10.1007/s00382-016-3263-8, 2017.
13. Frederiksen, J. S., & Frederiksen, C. S.: Interdecadal changes in Southern Hemisphere winter storm track modes, Tellus, 59 A, 599-617, 2007.
14. Frederiksen, J. S., Kitsios, V., O'Kane, T. J., & Zidikheri, M. J.: Stochastic subgrid modelling for geophysical and three-dimensional turbulence. In: *Nonlinear and Stochastic Climate Dynamics*, Chapter 9, 241–275, Franzke, C. J. E., & O'Kane, T. J. (Eds.), Cambridge University Press, 2016.
15. Frederiksen, J. S. & Webster, P. J.: Alternative theories of atmospheric teleconnections and low-frequency fluctuations, Rev. Geophys., 26, 459-494, 1988.
16. Ishijima, K., Nakazawa, T., & Aoki, S.: Variations of atmospheric nitrous oxide concentration in the northern and western Pacific, Tellus B, 61:2, 408–415, doi: 10.1111/j.1600-0889.2008.00406.x, 2009.
17. Kalnay, E., Kanamitsu, M., Kistler, R., Collins, W., Deaven, D., Gandin, L., Iredell, M., Saha, S., White, G., Woollen, J., Zhu, Y., Leetmaa, A., Reynolds, R., Chelliah, M., Ebisuzaki, W., Higgins, W., Janowiak, J., Mo, K. C., Ropelewski, C., Wang, J., Jenne, R., & Joseph, D.: The NCEP/NCAR Reanalysis 40-year Project, Bull. Amer. Meteor. Soc., 77, 437-471, 1996.
18. Keeling, R. F., Piper, S. C., Bollenbacher, A. F., and Walker, J. S.: Atmospheric CO_2 records from sites in the SIO air sampling network, In Trends: A Compendium of Data on Global Change. Carbon Dioxide Information Analysis Center, Oak Ridge National Laboratory, U.S. Department of Energy, Oak Ridge, Tenn., USA, 2009.
19. Keenan, T. F., Prentice, I. C., Canadell, J. G., Williams, C. A., Wang, H., Raupach, M. & Collatz, G. J.: Recent pause in the growth rate of atmospheric CO_2 due to enhanced terrestrial carbon uptake, Nature Communications, doi: 10.1038/ncomms13428, 2016.
20. Kim, W. M., Yeh, S. W., Kim, J. H., Kug, J. S., & Kwon, M. H.: The unique 2009–2010 El Niño event: A fast phase transition of warm pool El Niño to La Niña, Geophys. Res. Lett., 38, L15809, doi: 10.1029/2011GL048521, 2011.
21. Krol, M., de Bruine, M., Killaars, L., Ouwersloot, H., Pozzer, A., Yin, Y., Frederic Chevallier, F., Bousquet, P., Patra, P., Belikov, D., Maksyutov, S., Dhomse, S., Wuhu Feng, W., & Chipperfield, M. P.: Age of air as a diagnostic for transport time-scales in global models. Geosci. Model Dev. Discuss., doi: 10.5194/gmd-2017-262, 1–33, 2017.
22. Le Quéré, C., Andrew, R. M., Friedlingstein, P., Sitch, S., Pongratz, J., Manning, A. C., Korsbakken, J. I., Peters, G. P., Canadell, J. G., Jackson, R. B., Boden, T. A., Tans, P. P., Andrews, O. D., Arora, V. K., Bakker, D. C. E., Barbero, L.,

Becker, M., Betts, R. A., Bopp, L., Chevallier, F., Chini, L. P., Ciais, P., Cosca, C. E., Cross, J., Currie, K., Gasser, T., Harris, I., Hauck, J., Haverd, V., Houghton, R. A., Hunt, C. W., Hurtt, G., Ilyina, T., Jain, A. K., Kato, E., Kautz, M., Keeling, R. F., Klein Goldewijk, K., Körtzinger, A., Landschützer, P., Lefèvre, N., Lenton, A., Lienert, S., Lima, I., Lombardozzi, D., Metzl, N., Millero, F., Monteiro, P. M. S., Munro, D. R., Nabel, J. E. M. S., Nakaoka, S.-I., Nojiri, Y., Padín, X. A., Peregon, A., Pfeil, B., Pierrot, D., Poulter, B., Rehder, G., Reimer, J., Rödenbeck, C., Schwinger, J., Séférian, R., Skjelvan, I., Stocker, B. D., Tian, H., Tilbrook, B., van der Laan-Luijkx, I. T., van der Werf, G. R., van Heuven, S., Viovy, N., Vuichard, N., Walker, A. P., Watson, A. J., Wiltshire, A. J., Zaehle, S., & Zhu, D.: Global carbon budget 2017, Earth Syst. Sci. Data Discuss., 1–79, doi:10.5194/essd-2017-123, 2017.

23. L'Heureux, M. L.,Takahashi, K., Watkins, A. B., Barnston, A. G., Becker, E. J., Liberto, T. E., Gamble, F., Gottschalck, J., Halpert, M. S., Huang, B., Mosquera-Vásquez, K., & Wittenberg, A. T. : Observing and predicting the 2015/16 El Niño, Bull. Amer. Met. Soc., 98, 1363–1382, doi:10.1175/BAMS-D-16-0009.1, 2017.
24. Lintner, B. R., Gilliland, A. B., & Fung, I. Y.: Mechanisms of convection-induced modulation of passive tracer interhemispheric transport annual variability, J. Geophys. Res., 109, D13102, doi: 10.1029/2003JD004306, 2004.
25. Miyazaki, K., Patra, P. K., Takigawa, M., Iwasaki, T. & Nakazawa T.: Global-scale transport of carbon dioxide in the troposphere, J. Geophys. Res., 113, D15301, doi: 10.1029/2007JD009557, 2008.
26. NASA: Following carbon dioxide through the atmosphere, 2016. https://svs.gsfc.nasa.gov/12445
27. Ortega, S., Webster, P. J., Toma, V., & Chang, H. R.: The effect of potential vorticity fluxes on the circulation of the tropical upper troposphere, Quart. J. Roy. Met. Soc., doi: 10.1002/qj.3261, 2018.
28. Pandey, S., Houweling, S., Krol, M., Aben, I., Monteil, G., Nechita-Banda, N., Dlugokencky, E. J., Detmers, R., Hasekamp, O., Xu, X., Riley, W. J., Poulter, B., Zhang, Z., McDonald, K. C., James W. C. White, J. W. C., Philippe Bousquet, P., & Röckmann, T.: Enhanced methane emissions from tropical wetlands during the 2011 La Niña, Nature Scientific Reports 7, 45759, doi: 10.1038/srep45759, 2017.
29. Poulter, B., Frank, D., Ciais, P., Myneni, R. B., Andela, N., Bi, J., Broquet, G., Canadell, J. G., Chevallier, F., Liu, Y. Y., Running, S. W., Sitch, S., & Guido R. van der Werf, G. R.: Contribution of semi-arid ecosystems to inter-annual variability of the global carbon cycle, Nature, 509, 600–603, 2014.
30. Price, H., Jaegle´, L., Rice, A., Quay, P., Novelli, P. C., & Gammon, R.: Global budget of molecular hydrogen and its deuterium content: Constraints from ground station, cruise, and aircraft observations, J. Geophys. Res., 112, D22108, doi: 10.1029/2006JD008152, 2007.
31. Rienecker, M. M., Suarez, M. J., Gelaro, R., Todling, R., Bacmeister, J., Liu, E., Bosilovich, M. G., Schubert, S. D., Takacs, L., Kim, G. K., Bloom, S., Chen, J., Collins, D., Conaty, A., Da Silva, A., Gu, W., Joiner, J., Koster, R. D., Lucchesi, R., Molod, A., Owens, T., Pawson, S., Pegion, P., Redder, C. R., Reichle, R., Robertson, F. R., Ruddick, A. G., Sienkiewicz, M., & Woollen, J.: MERRA: NASA's modern-era retrospective analysis for research and applications, J. Clim. 24, 3624–3648, doi: 10.1175/JCLI-D-11-00015.1, 2011.

32. Rikus. L.: A simple climatology of westerly jet streams in global reanalysis datasets part 1: mid-latitude upper tropospheric jets, Clim. Dyn., 50, 2285–2310, doi: 10.1007/s00382-015-2560-y, 2018.
33. Stan, C., Straus, D.M., Frederiksen, J.S., Lin, H., Maloney, E.D. & Schumacher, C.: Review of tropical-extratropical teleconnections on intraseasonal time scales, Rev. Geophys., 55, 902-937, doi: 10.1002/2016RG000538, 2017.
34. Thoning, K. W., Tans, P. P. & Komhyr, W. D.: Atmospheric carbon dioxide at Mauna Loa Observatory, 2. Analysis of the NOAA/GMCC data, 1974 – 1985, J. Geophys. Res., 94, 8549–8565, 1989.
35. Trudinger, C. M., Haverd, V., Briggs, P. R., & Canadell, J. G.: Interannual variability in Australia's terrestrial carbon cycle constrained by multiple observation types, Biogeosciences, 13, 6363–6383, doi: 10.5194/bg-13-6363-2016, 2016.
36. Webster, P. J. & Holton, J. R.: Cross-equatorial response to mid-latitude forcing in a zonally varying basic state, J. Atmos. Sci.**,** 39, 722–733, 1982.
37. Yeh, S. W., Cai, W., Min, S. K., McPhaden, M. J., Dommenget, D., Dewitte, B., Collins, M., Ashok, K., An, S. I., Yim, B. Y., & Kug, J. S.: ENSO atmospheric teleconnections and their response to greenhouse gas forcing, Rev. Geophys., doi: 10.1002/2017RG000568, 2018.
38. Yue, C., Ciais, P., Bastos, A., Chevallier, F., Yin, Y., Rödenbeck, C., & Park, T.: Vegetation greenness and land carbon-flux anomalies associated with climate variations: a focus on the year 2015, Atmos. Chem. Phys., 17, 13903–13919, doi: 10.5194/acp-17-13903-2017, 2017.

Table captions

Table 1: Definitions of dynamical indices characterizing eddy and mean tracer transport.

Table 2: Correlations (r) between the detrended $C_{mlo\text{-}cgo}$ anomalies and indices of mean transport ω_H, ω_P, v_H and v_P averaged for Jun-Aug and Jun-Nov 1992-2016.

Table 3: Correlations (r) between the detrended mlo–cgo gas anomalies for CO_2, CH_4, CO and H_2 with CO_2 and u_{duct} index of transient transport averaged between Feb–Apr for 1992–2016. Also shown are corresponding correlations for N_2O and 1993-2016 and for SF_6 and 1998-2012.

Table 4: Correlations (r) between the detrended mlo–cgo gas anomalies for CO_2, CH_4, CO and H_2 with CO_2 and indices of mean transport, ω_P and v_P averaged between Jun–Aug for 1992–2016. Also shown are corresponding correlations for N_2O and 1993-2016 and for SF_6 and 1998-2012.

Figure captions

Figure 1: (a) OCO-2 image for 17 Feb 2015 showing Rossby wave dispersion (dashed red lines) in CO_2 concentration across the equator (dotted black line); the box labeled 'OCO-2 Satellite' shows the time period of the associated movie, (b) seasonal cycle of $C_{mlo\text{-}cgo}$ and u_{duct}, with area where both are positive shaded, for 1 Jan 2014 to 31 Dec 2016, and (c) 300 hPa wind vector directions and wind strength (ms^{-1}) on 17 Feb 2015.

Figure 2: (a) Annual average $C_{mlo-cgo}$ (solid) and global CO_2 emission estimate (dashed) for 1992 to 2016, (b) $C_{mlo-cgo}$ for boreal winter-spring (blue) and summer-autumn (orange), (c) u_{duct} for boreal winter-spring (blue) and summer-autumn (orange), (d) boreal summer-autumn ω_H (orange) and v_H (green).

Figure 3: Hovmoller diagrams of 300 hPa zonal wind (ms^{-1}) averaged between 5S and 5N as a function of longitude and time for (a) 1 January 2008 to 31 December 2010, (b) 1 January 2011 to 31 December 2013 and (c) 1 January 2014 to 31 December 2016. Green through to red represent westerly winds (u-winds, ms^{-1}) over the Western Hemisphere. White solid rounded rectangles denote the longitudinal extent of the Pacific duct and the height denotes the February to April period.

Figure 4: Correlation of vertical velocity ω (Pas^{-1}) at 300 hPa with SOI for Feb-Apr and 1948-2016.

Figure 5: Latitude height cross section of June to August 120E-240E average (a) ω (Pas^{-1}) – vertical velocity in pressure coordinates – for 1979-2016, (b) ω difference of 2016 minus 1979-2016, (c) ω difference of 2016 minus 2010.

Figure 6: Latitude height cross section of June to August 120E-240E average (d) meridional wind v (ms^{-1}) for 1979-2016, (e) meridional wind v difference of 2016 minus 1979-2016 and (f) meridional wind v difference of 2016 minus 2010.

Figure 7: (a) $C^*_{mlo-cgo}$ and $-u_{duct}$ averaged between Feb-Apr for 1992-2016 and (b) $C^*_{mlo-cgo}$, ω_P, ω_H, v_P and v_H averaged between Jun-Aug for 1992-2016 .

Figure 8: Time series of June–August and Annual averages of detrended mlo–cgo differences in CO_2 and H_2 and June–August average dynamical indices ω_P and v_P .

Tables

Table 1: Definitions of dynamical indices characterizing eddy and mean tracer transport.

Dynamical index	Definition
u_{duct}	Average 300 hPa zonal velocity in the region 5°N to 5°S, 140°W to 170°W.
ω_H	Average 300 hPa vertical velocity in pressure coordinates in the region 10°N to 15°N, 0 to 360E.
v_P	Average 200 hPa meridional velocity in the region 5°N to 10°N, 0 to 360E.
ω_P	Average 300 hPa vertical velocity in pressure coordinates in the region 10°N to 15°N, 120E to 240E.
v_H	Average 200 hPa meridional velocity in the region 10°N to 15°N, 120E to 240E.

Table 2: Correlations (r) between the detrended $C_{mlo\text{-}cgo}$ anomalies and indices of mean transport ω_H, ω_P, v_H and v_P averaged for Jun-Aug and Jun-Nov 1992-2016.

Time Period	ω_H	ω_P	v_H	v_P
Jun-Aug	$r = 0.361$	$r = 0.522$	$r = 0.235$	$r = 0.539$
Jun-Nov	$r = 0.297$	$r = 0.481$	$r = 0.355$	$r = 0.355$

Table 3: Correlations (r) between the detrended mlo–cgo gas anomalies for CO_2, CH_4, CO and H_2 with CO_2 and u_{duct} index of transient transport averaged between Feb–Apr for 1992–2016. Also shown are corresponding correlations for N_2O and 1993-2016 and for SF_6 and 1998-2012.

Gas	CO_2	u_{duct}
CO_2	$r = 1.0$	$r = -0.500$
CH_4	$r = 0.697$	$r = -0.448$
CO	$r = 0.645$	$r = -0.605$
H_2	$r = 0.296$	$r = -0.218$
N_2O	$r = 0.215$	$r = -0.088$
SF_6	$r = 0.619$	$r = -0.617$

Table 4: Correlations (r) between the detrended mlo–cgo gas anomalies for CO_2, CH_4, CO and H_2 with CO_2 and indices of mean transport, ω_P and v_P averaged between Jun–Aug for 1992–2016. Also shown are corresponding correlations for N_2O and 1993-2016 and for SF_6 and 1998-2012.

Gas	CO_2	ω_P	v_P
CO_2	$r = 1.0$	$r = 0.522$	$r = 0.539$
CH_4	$r = 0.246$	$r = 0.195$	$r = 0.250$
CO	$r = 0.108$	$r = 0.205$	$r = 0.236$
H_2	$r = 0.680$	$r = 0.427$	$r = 0.442$
N_2O	$r = -0.010$	$r = 0.290$	$r = 0.266$
SF_6	$r = 0.223$	$r = 0.433$	$r = 0.385$

5

Figures

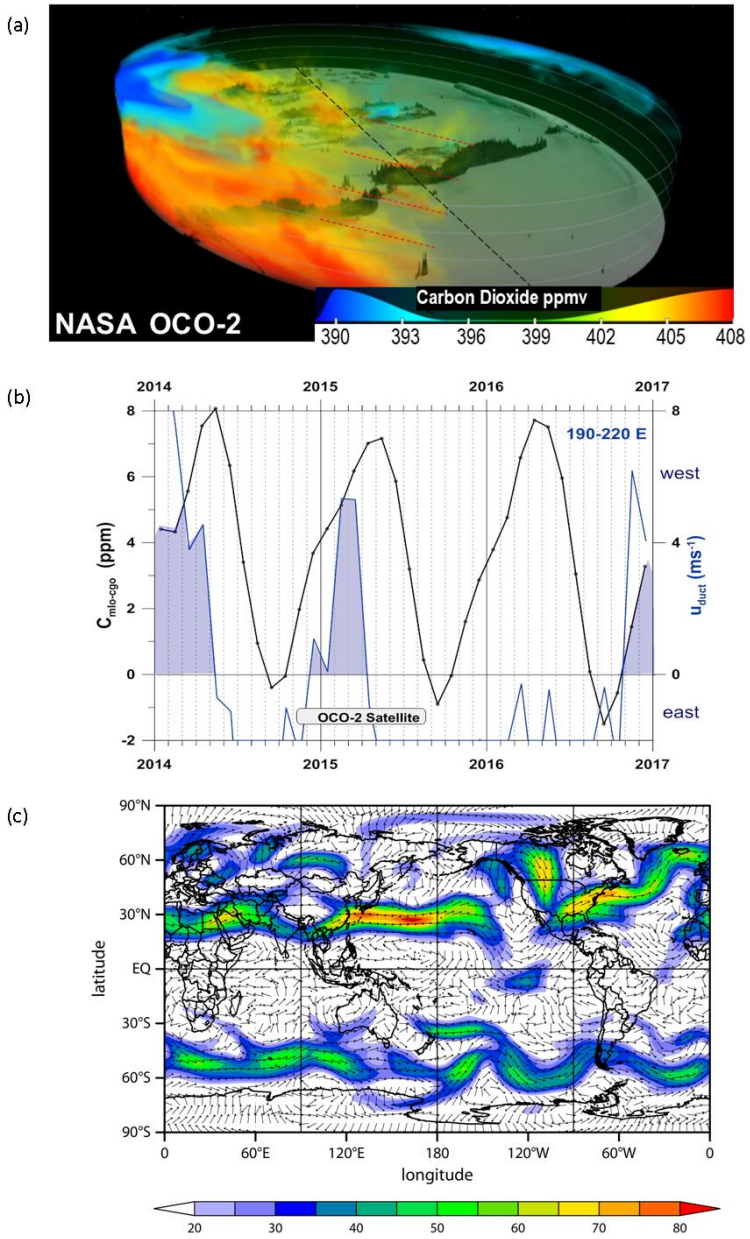

Figure 1: (a) OCO-2 image for 17 Feb 2015 showing Rossby wave dispersion (dashed red lines) in CO_2 concentration across the equator (dotted black line); the box labeled 'OCO-2 Satellite' shows the time period of the associated movie , (b) seasonal cycle of $C_{mlo-cgo}$ and u_{duct}, with area where both are positive shaded, for 1 Jan 2014 to 31 Dec 2016, and (c) 300 hPa wind vector directions and wind strength (ms^{-1}) on 17 Feb 2015.

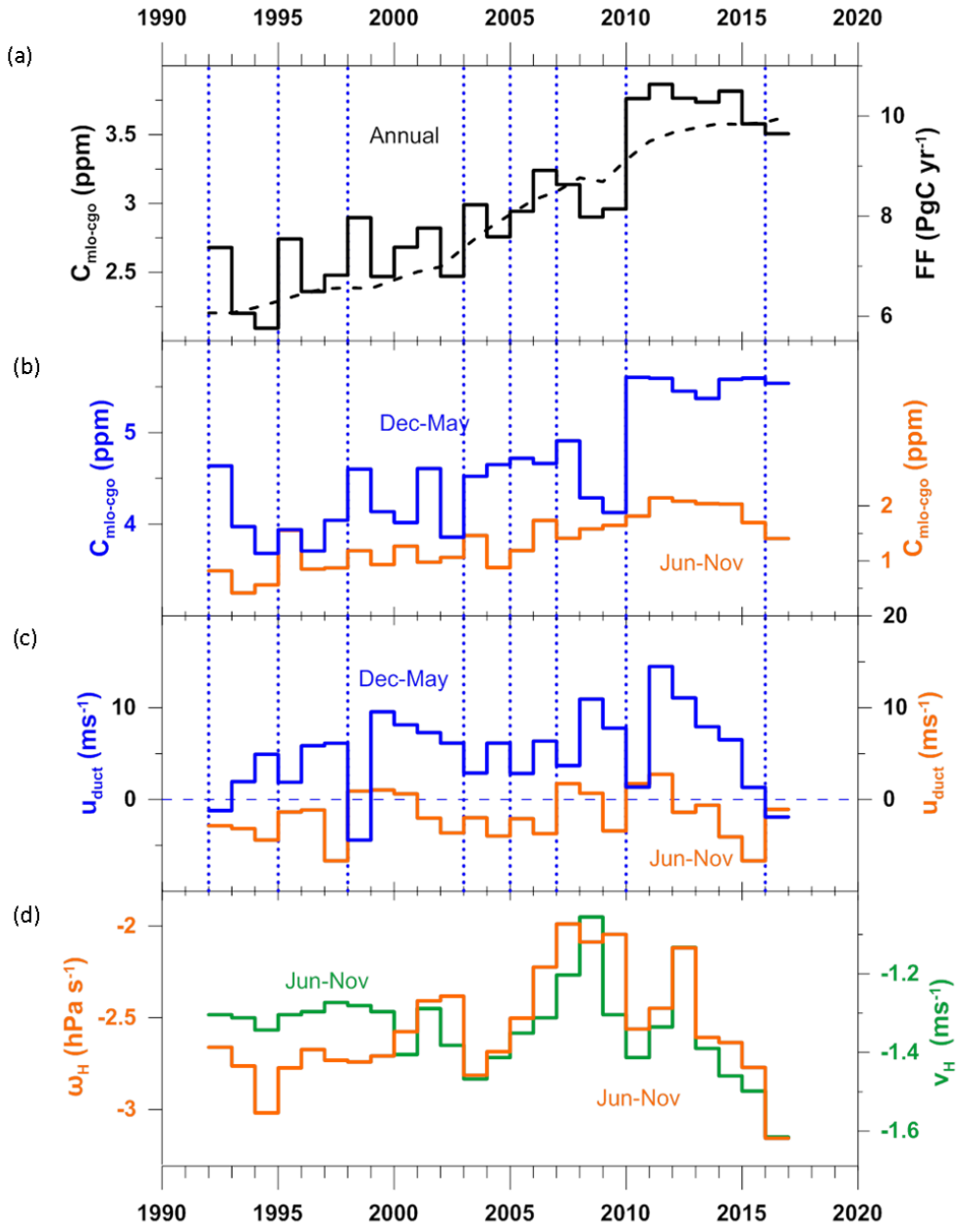

Figure 2: (a) Annual average $C_{mlo-cgo}$ (solid) and global CO_2 emission estimate (dashed) for 1992 to 2016, (b) $C_{mlo-cgo}$ for boreal winter-spring (blue) and summer-autumn (orange), (c) u_{duct} for boreal winter-spring (blue) and summer-autumn (orange), (d) boreal summer-autumn ω_H (orange) and v_H (green).

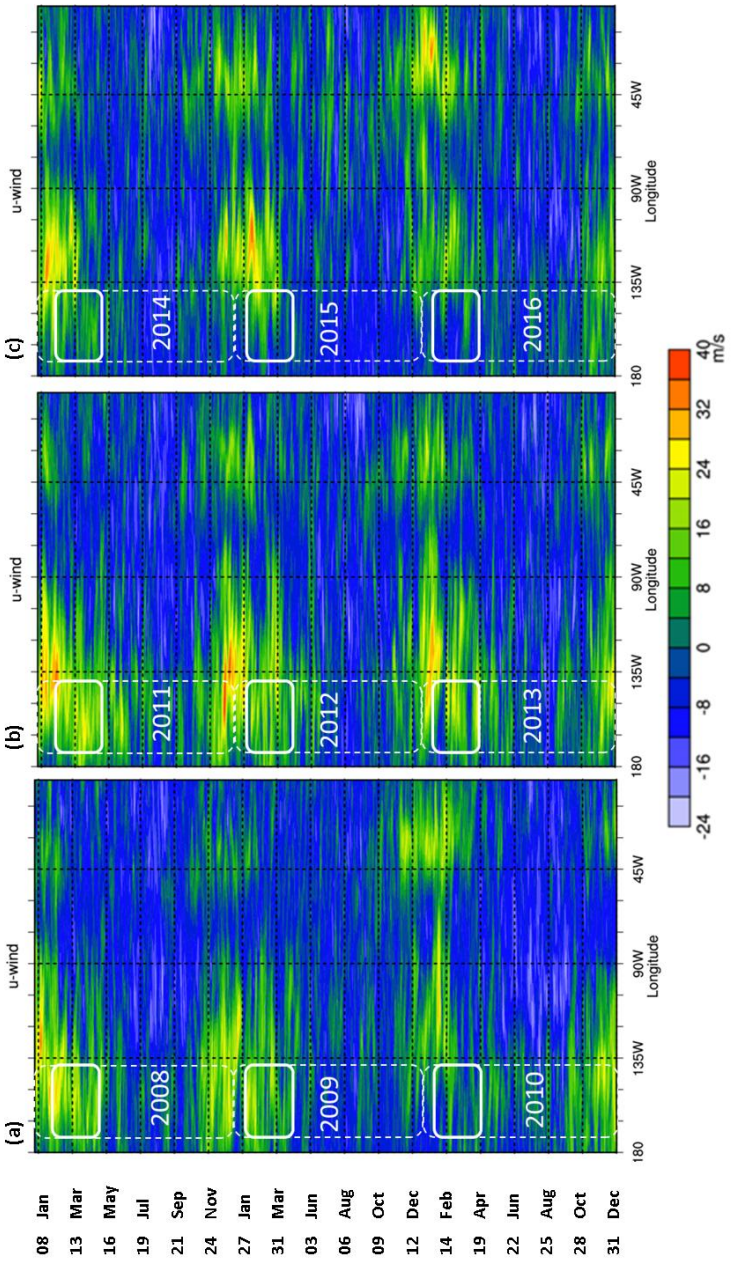

Figure 3: Hovmoller diagrams of 300 hPa zonal wind (ms^{-1}) averaged between 5S and 5N as a function of longitude and time for (a) 1 January 2008 to 31 December 2010, (b) 1 January 2011 to 31 December 2013 and (c) 1 January 2014 to 31 December 2016. Green through to red represent westerly winds (u-winds, ms^{-1}) over the Western Hemisphere. White solid rounded rectangles denote the longitudinal extent of the Pacific duct and the height denotes the February to April period.

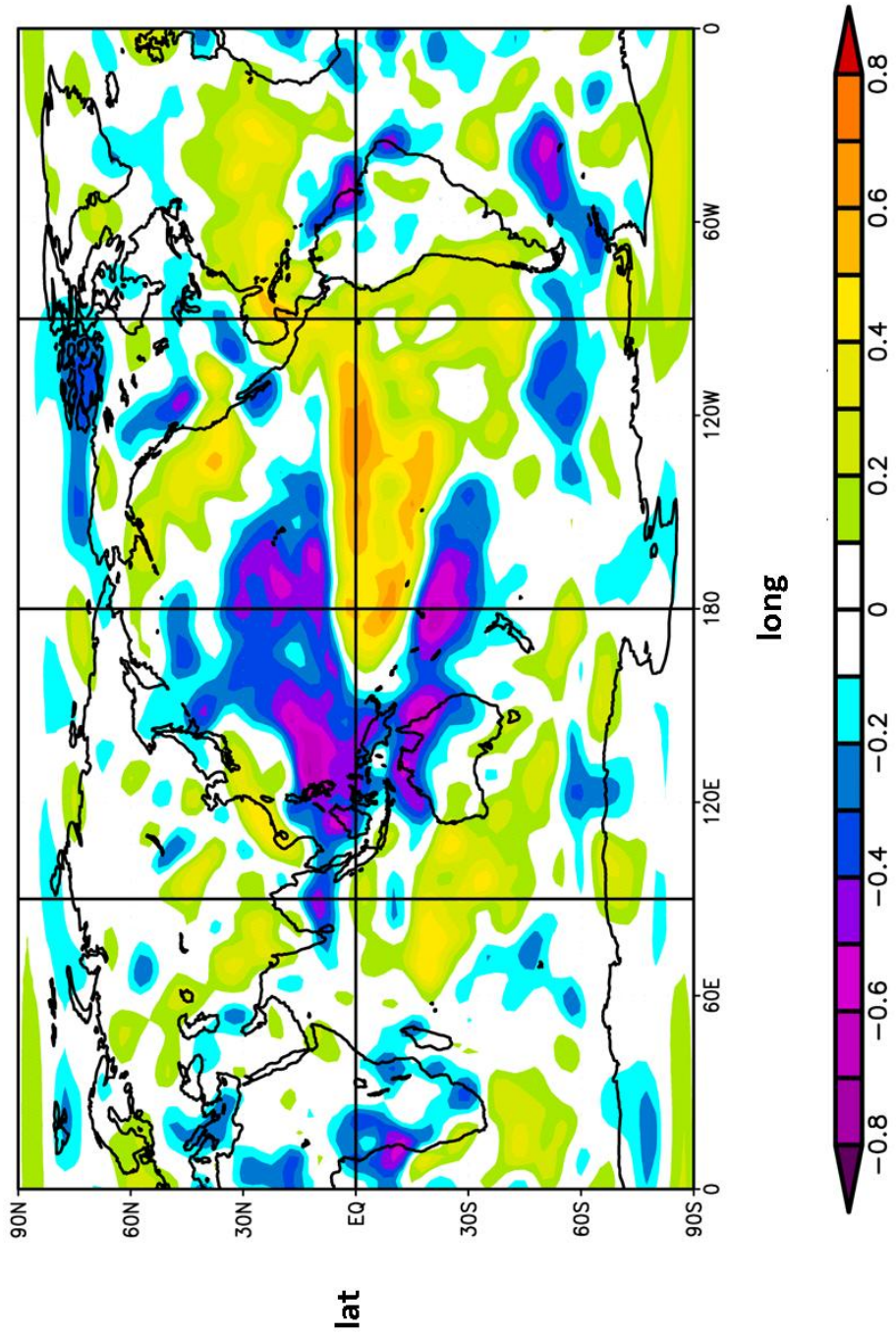

Figure 4: Correlation of vertical velocity ω (Pas^{-1}) at 300 hPa with SOI for Feb-Apr and 1948-2016.

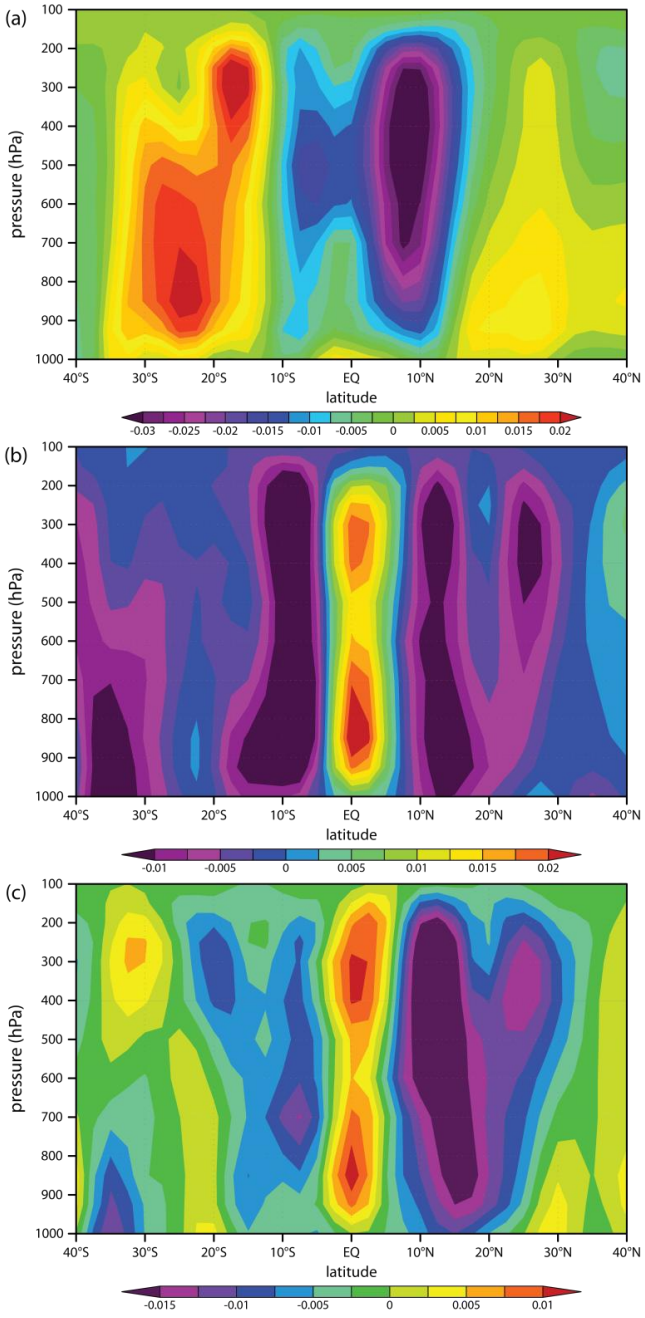

Figure 5: Latitude height cross section of June to August 120E-240E average (a) ω (Pas^{-1}) – vertical velocity in pressure coordinates – for 1979-2016, (b) ω difference of 2016 minus 1979-2016, (c) ω difference of 2016 minus 2010.

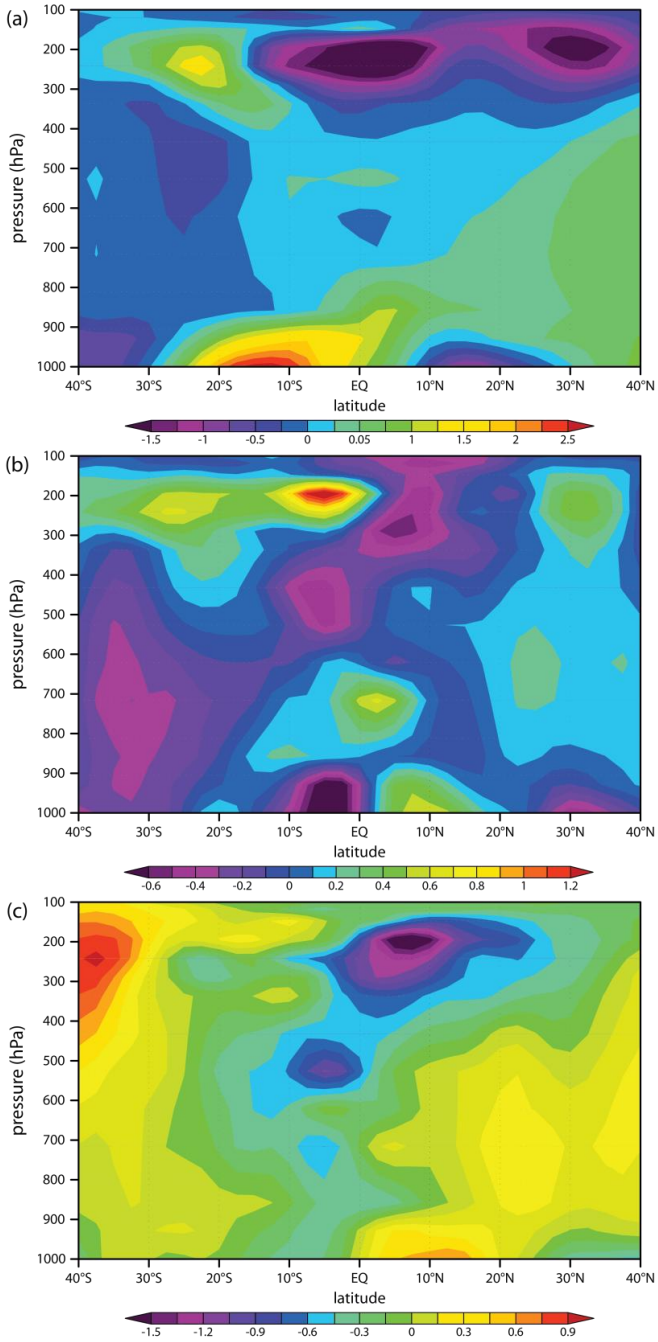

Figure 6: Latitude height cross section of June to August 120E-240E average (d) meridional wind v (ms^{-1}) for 1979-2016, (e) meridional wind v difference of 2016 minus 1979-2016 and (f) meridional wind v difference of 2016 minus 2010.

5

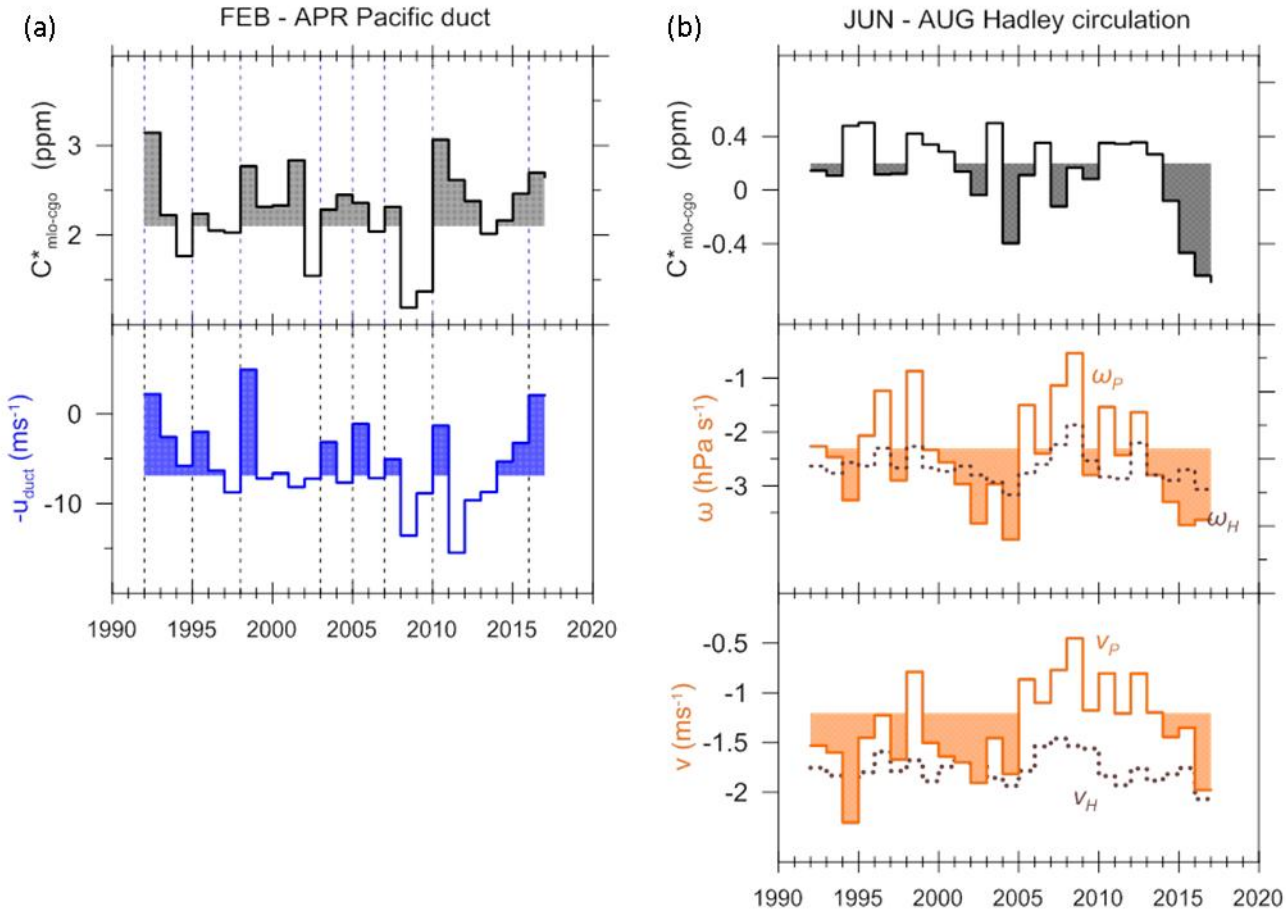

Figure 7: (a) $C^*_{mlo\text{-}cgo}$ and $-u_{duct}$ averaged between Feb-Apr for 1992-2016 and (b) $C^*_{mlo\text{-}cgo}$, ω_P, ω_H, v_P and v_H averaged between Jun-Aug for 1992-2016 .

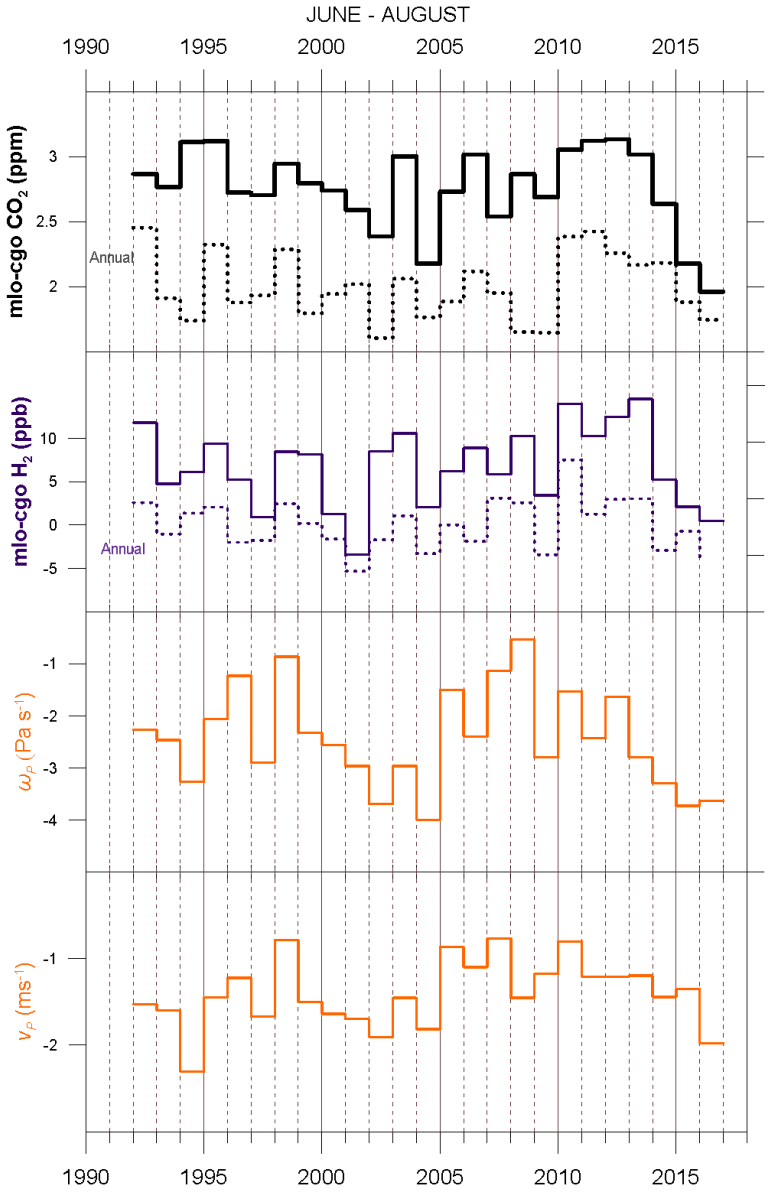

Figure 8: Time series of June–August and Annual averages of detrended mlo–cgo differences in CO_2 and H_2 and June–August average dynamical indices ω_P and v_P .